

# Emission line properties of the most luminous AGN in massive galaxies at intermediate redshifts

Guinevere Kauffmann<sup>1\*</sup>, Claudia Maraston<sup>2</sup>

<sup>1</sup>*Max-Planck Institut für Astrophysik, 85741 Garching, Germany*

<sup>2</sup>*Institute of Cosmology and Gravitation, Dennis Sciama Building, Burnaby Road, Portsmouth PO1 3FX, UK*

15 August 2019

## ABSTRACT

We have analyzed the emission line properties of 6019 Type II AGN at redshifts between 0.4–0.8 with [OIII] luminosities greater than  $3 \times 10^8 L_{\odot}$ , characteristic of the Type II quasars first identified in population studies by Zakamska et al (2003). The AGN are drawn from the CMASS sample of galaxies with stellar masses greater than  $10^{11} M_{\odot}$  that were studied as part of the Baryon Oscillation Spectroscopic Survey (BOSS) and comprise 0.5% of the total population of these galaxies. Individual spectra have low S/N, so the analysis is carried out on stacked spectra in bins of [OIII] luminosity and estimated stellar age. The emission line ratios of the stacks are well fit with simple uniform-density photoionization models with metallicities between solar and twice solar. In the stacks, a number of emission lines are found to have distinct broad components requiring a double Gaussian rather than a single Gaussian fit, indicative of outflowing ionized gas. These are: [OIII] $\lambda$ 4959, [OIII] $\lambda$ 5007, [OII] $\lambda$ 3727,3729 and H $\alpha$  $\lambda$ 6563. Higher ionization lines such as [NeIII] $\lambda$ 3869 and [NeV] $\lambda$ 3345 are detected in the stacks, but are well fit by single Gaussians. The broad components typically contain a third of the total line flux and have widths of 600 km/s for the oxygen lines and 900 km/s for H $\alpha$ . The fraction of the flux in the broad component and its width are independent of [OIII] luminosity, stellar age, radio and mid-IR luminosity. The stellar mass of the galaxy is the only parameter we could identify that influences the width of the broad line component.

**Key words:** galaxies:active; galaxies:formation; galaxies:ISM; galaxies:star formation

## 1 INTRODUCTION

Emission lines from ionized gas in active galactic nuclei (AGN) have long served as probes of the physical conditions of gas in the vicinity of the actively accreting black holes in these systems (see Osterbrock 1989 for a review). In Type I AGN, much of the emission originates very close to the black hole from gas in the accretion disk (Shakura & Sunyaev 1973). In Type II AGN, the accretion disk is obscured by dust and the emission lines probe highly ionized gas within the host galaxy (Antonucci 1993).

A standard analysis technique is to compare observed emission line strengths with photo-ionization models in order to constrain physical conditions within the gas. Baldwin, Phillips and Terlevich (1981) pointed out the importance of the [OIII] $\lambda$ 5007/H $\beta$  versus [NII] $\lambda$ 6584/H $\alpha$  diagram (hereafter the BPT diagram) for classifying emission-line galaxies as either active galactic nuclei or star-forming systems. In addition to the mechanism responsible for the excitation of

the gas, emission line ratio diagrams provide important information about the spectrum of the ionizing source, as well as gas temperature, density and metallicity. Line ratios also constrain the structure of the gas. e.g. whether it is in the form of radiation pressure dominated dusty clouds (Groves et al 2004a,b) or matter and ionization-bounded clouds (Binnette et al 1996).

Emission line shapes provide additional important information about the kinematics of the ionized gas in the galaxy. A large body of recent work has focused on signatures of outflowing gas in powerful AGN, both at intermediate and at high redshifts. The most detailed of these studies are based on Integral Field Unit (IFU) spectroscopy. In a series of papers, Liu et al (2013a,b) studied ionized gas nebulae in samples of around a dozen luminous, obscured, radio-quiet quasars at  $z \sim 0.5$  by means of Gemini Integral Field Unit observations of the [OIII] $\lambda$ 5007 Å line. The nebulae were found to have round morphologies and a mean diameter of 28 kpc. At each position within the nebulae, the velocity structure of the [OIII] $\lambda$ 5007 Å line was found to be complex. The complicated line shapes were hypothesized

\* E-mail: gamk@mpa-garching.mpg.de

to reflect the existence of multiple gas components whose three-dimensional velocities are projected onto the line-of-sight. Liu et al (2014) showed that the line shapes could be well described by a superposition of 2-3 Gaussians. In some of the lines-of-sight through the nebulae, there was a blueshifted excess in the line profile and in others, there was a redshifted excess, signifying that a significant fraction of the gas is outflowing, rather than in a pressure-supported spherically symmetric cloud of halo gas around the central nucleus. The observed velocity widths were used to estimate a median outflow velocity of 760 km/s.

Multi-Gaussian component fitting has by now become a standard technique to study outflowing ionized gas in galaxies and has been applied extensively to samples of both star-forming and active galaxies of different types (Genzel et al (2011) (star-forming clumps in z-2 galaxies); Harrison et al 2017 (x-ray AGN); Talia et al 2017; Davies et al 2019 (high-z star-forming galaxies); Toba et al 2017 (IR bright dust-obscured galaxies); Schmidt et al (2018) (narrow-line Seyfert I); Zakamska et al (2016) (high-z red quasars); Rose et al 2018 (ULIRGS).

As the samples under study have increased in size, comparative studies between the emission line properties of different types of objects, studies of systematic trends in outflow properties as a function of star formation rate or AGN luminosity, and comparisons of outflow signatures traced by a variety of different gas tracers have become possible. Some of the main findings so far are that at fixed luminosity, obscured and unobscured AGN have very similar ionized gas nebulae sizes and kinematics (Liu et al 2014; Harrison et al 2018). At fixed redshift, high outflow velocities are typical of AGN, but are rarely found in star-forming galaxies (Harrison et al (2018). Forster-Schreiber et al (2019)) find that the faster AGN-driven outflows become dominant in host galaxies with stellar masses  $\log M_* > 10.7$  and are found in 75% of all emission line galaxies with  $\log M_* > 11.2$ . Outflows traced by ionized/neutral gas and by molecular gas have now been compared in a sample of a dozen galaxies by Fluetsch et al (2019). In star forming galaxies, the ionized outflow is estimated to carry as much total mass as the molecular outflow, but in AGN, the molecular component dominates (see also a recent high-resolution comparison of molecular and H $\alpha$  outflow components in a massive galaxy at z=2 by Herrera-Camus et al (2018)).

In this paper we have carried out a systematic study of the emission lines in the most luminous AGN found in the CMASS sample of galaxies observed as part of the SDSS-III survey (Padmanabhan et al. 2012). The parent sample consists of around a million galaxies in the redshift range  $0.4 < z < 0.8$  with median stellar mass of around  $3 \times 10^{11} M_\odot$ . The majority of these galaxies are thus massive “red-and-dead” galaxies, but the adopted colour cuts do not exclude systems with ongoing star formation and emission lines. The S/N of individual spectra is low, but [OIII] can be reliably detected at luminosities greater than  $3 \times 10^8 L_\odot$ , which corresponds to the threshold [OIII] luminosity for an AGN to be included in catalogues of type II quasar systems (Zakamska et al 2003). Redshift templates for galaxies are constructed by performing a rest-frame principal-component analysis (PCA) of training samples of known redshift. The leading eigenspectra from the PCA results are used to define a linear template basis that is used to model the spectra in

the redshift analysis. Statistical redshift errors propagated from photon noise are typically a few tens of km/s for galaxies (Bolton et al 2012). We adopt these pipeline redshifts as the systemic velocity of the AGN in the analysis that follows.

In recent work, Kauffmann (2018) studied a sample of nearby AGN with comparable luminosities and showed that unlike the much more numerous low-luminosity systems, the host galaxies of these object exhibited clear signatures of recent starbursts and mergers/interactions. Although few in number, they are responsible for the bulk of the recent black hole growth in the most massive galaxies. In this work, by stacking spectra of comparable higher redshift systems in bins of [OIII] luminosity and estimated mean stellar age, we recover very high S/N composite AGN spectra and study trends in emission line ratios and shapes as a function of these two quantities. We can also select subsamples that are detected in the Faint Images of the Radio Sky at Twenty cm (FIRST) survey (Becker, White & Helfand 1995) or Wide-field Infrared Survey Explorer (WISE) survey (Wright et al 2010) to investigate whether radio-loud, dusty sources differ systematically in their emission line properties. In this way, we hope to gain insight into the physical mechanisms responsible for signatures of outflowing gas.

Our paper is structured as follows. In section 2, we describe our sample selection, stacking and line-fitting procedure. In section 3, we show how emission line ratios vary as a function of [OIII] luminosity and mean stellar age and we compare our derived sequences of emission line ratios to available grids of photo-ionization models by Groves et al (2004). In section 4, we carry out an examination of emission lines in a small sample of very luminous AGN in the nearby Universe. In section 5, we move onto an analysis of the emission lines shapes in the composite spectra as quantified by multi-Gaussian line fitting. In section 6, we conclude by summarizing our results and discussing future perspectives.

## 2 SAMPLE SELECTION AND LINE-FITTING

### 2.1 Sample construction

Our parent sample is constructed from the Wisconsin catalogue of principal component analysis (PCA)-based stellar masses and velocity dispersions that has been publicly released for the data release 12 (DR12) of the SDSS (Alam et al 2015). The methodology for deriving stellar masses and other physical parameters from the spectra is described in detail in Chen et al (2012). In brief, the steps in the method are as follows. A library of model star formation histories is generated with a range in parameters such as the e-folding time of SFR(t), the recent burst mass fraction, the metallicity of the stellar population, and the amount of dust extinction. Principal components (PCs) are identified from the model library after subtraction of the mean spectrum calculated from the entire library. Physical parameters are estimated after projecting the observed spectrum onto the PCs. A weight  $w_i = \exp(-\chi_i^2/2)$  is defined to describe the similarity between the given galaxy and model  $i$  and a probability distribution function (PDF) is then built for each parameter P, by looping over all the model galaxies in the library and by summing the weights  $w_i$  at the value of

P for each model. A set of 7 PCs are provided in the Wisconsin catalogue, from which it is possible to reconstruct a variety of physical parameters (see Table 1 of Chen et al (2012)). In this paper, we make use of the stellar mass and the estimated mean stellar age of the stellar population. We note that the model-fitting assumes the universal initial mass function (IMF) given in Kroupa (2001).

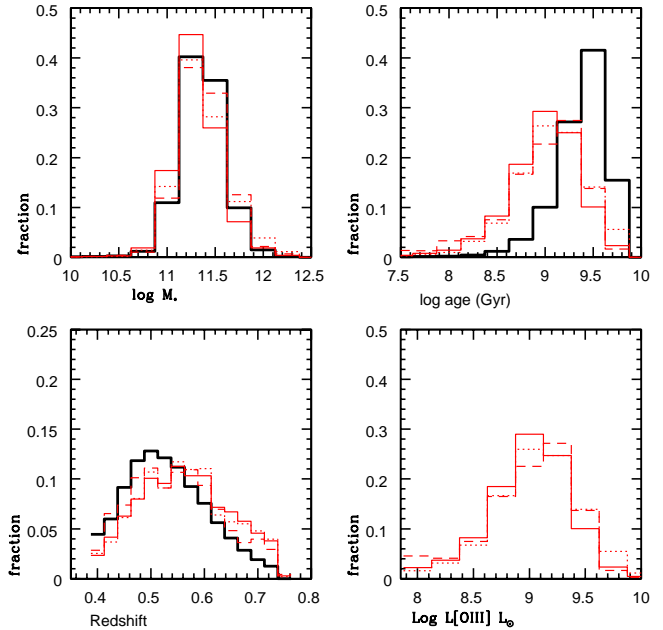
We select all galaxies from the catalogue in the redshift range  $0.4 < z < 0.75$ , yielding a sample of 1,094,697 galaxies. Almost all of these galaxies are included in the ‘‘CMASS’’ sample, so-named because it is very approximately stellar-mass limited even though it is selected by colour (Padmanabhan et al 2012). These are then cross-correlated with the Portsmouth catalogue of stellar kinematics and emission line fluxes (Thomas et al 2013), which uses adaptations of the publicly available codes Penalized PiXel Fitting (pPXF, Cappellari & Emsellem 2004) and Gas and Absorption Line Fitting code (GANDALF v1.5; Sarzi et al. 2006) to calculate stellar kinematics and to derive emission line properties. We find 6019 galaxies with [OIII] $\lambda$ 5007 line luminosities greater than  $3 \times 10^8 L_{\odot}$  (i.e 0.5% of the parent sample). In 94% of these systems, the [OIII] line is detected with  $S/N > 3$  and in 78%, it is detected with  $S/N > 5$ , i.e. the [OIII] line luminosity can be measured in all these galaxies with reasonable accuracy.

Figure 1 shows histograms of stellar masses, redshift, mean stellar ages, and [OIII] luminosities for the parent sample (solid black histograms) and [OIII]-detected galaxies (red histograms)<sup>1</sup>. We have created sub-samples of [OIII]-detected objects with radio source counterparts in the FIRST VLA survey (dashed red histograms) and with detections in the W1 and W2 bands in the WISE source catalogue (dotted red histograms). As can be seen, all of the samples have very similar distributions of stellar masses. The [OIII]-detected samples are shifted to higher redshifts and lower mean stellar ages compared to the parent sample. The shift to higher redshift occurs because CMASS galaxies are selected a fixed limited magnitude in the *i*-band and the [OIII] line is redshifted through this bandpass over the redshift interval spanned by the galaxies in this sample. The shift to younger ages is in accord with the findings of Kauffmann et al (2003b) that luminous AGN have younger stellar ages than control galaxies of the same stellar mass and morphological type. The radio and WISE-detected subsamples do not differ significantly in [OIII] line luminosity or mean stellar age compared to the full [OIII]-detected sample.

## 2.2 Stacking procedure

We divide our sample of 6019 galaxies into 3 bins in [OIII] line luminosity:  $\log L[\text{OIII}] = 8.5\text{-}9.0$ ;  $9.0\text{-}9.5$ ;  $9.5\text{-}10.0$ , and 4 bins in mean stellar age:  $\log \text{age}(\text{yr}) = 8.0\text{-}8.4$ ,  $8.4\text{-}8.8$ ,  $8.8\text{-}9.2$ , and  $9.2\text{-}9.6$ . Emission lines are usually quite weak in the oldest bin, so in some cases we will only show results for a total of 9 stacked spectra rather than 12. The number of galaxies in each bin range from  $\sim 50$  in the highest luminosity bins to  $\sim 1500$  in the lower luminosity ones.

Our stacking methodology follows the procedure laid



**Figure 1.** Histograms of the fraction of galaxies as a function of stellar mass, redshift, mean stellar age, and [OIII] luminosity for the parent sample (solid black histograms) and for [OIII]-detected galaxies with [OIII] luminosities greater than  $10^8 L_{\odot}$  (solid red histograms). Results are also plotted for sub-samples of [OIII]-detected objects with radio source counterparts in the FIRST VLA survey (dashed red histograms) and with detections in the W1 and W2 bands in the WISE source catalogue (dotted red histograms).

out in Vanden Berk et al (2001), who created a variety of composite quasar spectra using a homogeneous data set of over 2200 spectra from the Sloan Digital Sky Survey (SDSS). We first mask skylines and bad pixels in each spectrum and interpolate the flux over the masked pixels. The spectra are rebinned onto a  $1 \text{ \AA}$  linear grid in rest-frame wavelength. The spectra are ordered in redshift from lowest to highest. The stacking then proceeds as follows. The rest-frame wavelength boundaries of spectrum( $N=i$ ) are determined and the mean flux is calculated over these boundaries. The mean flux of spectra( $N=1\dots i-1$ ) is then computed over the same wavelength boundaries and the mean flux spectrum( $n=i$ ) is rescaled by a constant factor such that they match. In this way, every spectrum in the stack carries equal weight, regardless of the redshift or the luminosity of the source. We have calculated both mean and median stacks of the flux and find that emission lines are stronger in the mean stacks, so these are utilized in this paper. As we will show, the emission line shapes do not depend strongly on the luminosity of the AGN in the stack, so using mean stacks will not bias our results. Finally, we boxcar smooth the spectra to a resolution of  $3 \text{ \AA}$  and calculate the error on the mean spectrum by a boot-strap resampling process where the stacking is repeated 100 times on randomly selected spectra drawn from the given bin of [OIII] luminosity and mean stellar age.

<sup>1</sup> In this plot we show all galaxies with [OIII] detected down to a limiting line luminosity of  $10^8 L_{\odot}$ .

### 2.3 Continuum fitting

For continuum fitting, we have implemented the algorithm described in Wilkinson et al (2017), who introduced a code called FIREFLY (Fitting Iteratively for Likelihood analysis). The method is based on fitting combinations of single stellar populations (SSPs), following an iterative, best-fitting process until convergence is reached based on a Bayesian Information Criterion. The algorithm is described in detail in Section 3.2 of Wilkinson et al, and so we will not provide a detailed description of all the steps here.

In order to span as wide a wavelength range as possible in the spectral fitting, we use the stellar population models of Maraston & Stromback (2011), which have been extended into the UV using the theoretical spectral library UVBLUE (Rodrigues-Merino et al. 2005). We note that the first version of the UV-extended models were published in Maraston et al (2009) and included fully theoretical, high-resolution SEDs for wavelengths  $\lambda < 4350 \text{ \AA}$ . The optical part of the SSPs are constructed using the MILES stellar library (Sánchez-Blazquez et al 2006), which provides observed spectra for 1000 stars covering most evolutionary stages. In our fitting procedure, we utilize SSPs that span a range in ages from 0.055 to 12 Gyr at half solar, solar and twice solar metallicities – this should cover the likely range of metallicities in massive galaxies with  $\log M_* \sim 11$ . Once again, a Kroupa (2001) IMF has been adopted.

The SSPs are convolved with a Gaussian function with  $\sigma=200 \text{ km/s}$  to match the typical velocity dispersion of the galaxies in our sample and then boxcar smoothed to the same  $3 \text{ \AA}$  resolution as the real stacked spectra. Regions around known emission lines are masked before carrying out the fitting. We implement the two-parameter dust extinction model of Wild et al (2007) on each SSP, which has the form:

$$\tau_\lambda/\tau_v = (1 - \mu)(\lambda/5500\text{\AA})^{-1.3} + \mu(\lambda/5500\text{\AA})^{-0.7} \quad (1)$$

where  $\tau_v$  is the total effective optical depth in the V-band and  $\mu$  is the fraction of the total optical depth contributed by the ambient interstellar medium. This form of extinction law is motivated by the dust model of Charlot & Fall (2000) and has been shown to be broadly consistent with observational determinations (Wild et al 2011). We allow  $\mu$  to span the full range from 0 to 1 and  $\tau_v$  to vary from 0 to 3. Note that each fitted SSP is allowed to have different values of  $\tau_v$  and  $\mu$ . In practice we find that our AGN spectra are best fit by combining old SSPs with low dust extinction with young SSPs with high dust extinction, as would be expected if these systems are undergoing or have undergone a recent burst of star formation.

An example of a continuum fit is shown in Figure 2 for the stack with  $\log L[\text{OIII}]=8.5$  and mean stellar age between  $6.3 \times 10^8$  and  $1.5 \times 10^9$  Gyr. The stacked spectrum is plotted in black, with vertical black lines delineating masked regions of the spectrum (the actual emission lines in the stacked spectrum are shown in blue). The cyan bands across the bottom of each of the panels indicate the  $\pm 1\sigma$  errors on the mean observed flux. The best fit model spectrum is shown in red. Note that the rest-frame wavelength range over which the SSP model fitting is carried out is 2500-7000  $\text{\AA}$  and Figure 2 shows that there is a good match to the continuum level across this entire interval.

### 2.4 Line fitting

We carry out emission line fitting in a series of iterative steps of increasing complexity. In order of increasing wavelength, the emission lines that are generally well-detectable in most of the stacked spectra are:  $[\text{Mg II}]\lambda 2796, 2803$ ,  $\text{HeII}\lambda 3203$ ,  $[\text{NeV}]\lambda 3345$ ,  $[\text{OII}]\lambda 3726, 3728$ ,  $[\text{NeIII}]\lambda 3869$ ,  $\text{H}\delta\lambda 4102$ ,  $\text{H}\gamma\lambda 4340$ ,  $[\text{OIII}]\lambda 4363$ ,  $[\text{HeII}]\lambda 4686$ ,  $\text{H}\beta\lambda 4861$ ,  $[\text{OIII}]\lambda 4959$ ,  $[\text{OIII}]\lambda 5007$ ,  $[\text{OI}]\lambda 6300$ ,  $\text{H}\alpha\lambda 6563$ ,  $[\text{NII}]\lambda 6583$ .

The first step is to subtract the best-fit continuum, and to perform a fit to the line using a single Gaussian, with line amplitude, width and centroid as free parameters (the centroid can vary within  $\pm 10 \text{ \AA}$  of the rest-frame wavelength). Even after subtraction of the best-fit continuum, a small systematic offset from zero is sometimes found at large wavelength separation from the line centroid, indicative of a systematic error in the continuum estimate. These offsets are usually very small compared to the peak flux of the line ( $< 1\%$  in all cases). We allow for a constant additive correction to the best-fit continuum, refit the line and adopt this as our corrected continuum if  $\chi^2$  has decreased. The next step is to perform a double Gaussian fit. In the first instance, we adopt the same centroid for the secondary component as derived for the single Gaussian fit. If  $\chi^2$  decreases by 30% or more, then we record the secondary component as a clear detection. Finally, we refit the double Gaussian allowing the centroid of the secondary component to vary to obtain final parameter values for both components.

As we will show in Section 5, either one or two Gaussian components are sufficient to fit nearly all the lines in the stack. In the case of two closely spaced lines, line-fitting results from one line may need to be included when fitting the second one. For example, in the case of  $[\text{OIII}]\lambda 4959$  and  $[\text{OIII}]\lambda 5007$ , we fit the weaker 4959 line first. In almost all cases, a clear broad component is detected and careful subtraction of its contribution redward of the line centroid is necessary before a fit to  $[\text{OIII}]\lambda 5007$  can be performed. We will illustrate the case of the  $\text{H}\alpha/[\text{NII}]$  complex in more detail in Section 5.

## 3 EMISSION LINE RATIO TRENDS AS A FUNCTION OF $[\text{OIII}]$ LUMINOSITY AND AGE

After fitting and subtracting the emission lines from the stacked spectrum, we measure the age-sensitive stellar continuum indices  $D_n(4000)$  (the narrow version of the 4000  $\text{\AA}$  break strength defined in Balogh et al (1999)) and the  $\text{H}\delta_A$  Lick index defined in Worthey & Ottaviani (1997). In Figure 3, the top two panels show the measured values of  $D_n(4000)$  and  $\text{H}\delta_A$  as a function of the logarithm of the mean stellar age. Each stellar age bin is indicated by a filled square. Results are shown in different colours for the 3 different bins in  $\log L[\text{OIII}]$ : green ( $\log L[\text{OIII}]=8.5-9$ ); red ( $\log L[\text{OIII}]=9-9.5$ ); magenta ( $\log L[\text{OIII}]=9.5-10$ ). The relation between  $D_n(4000)$  and stellar age is independent of  $[\text{OIII}]$  luminosity, but  $\text{H}\delta_A$  is considerably stronger at ages between a few  $\times 10^8$  years and  $10^9$  years in the more  $[\text{OIII}]$ -luminous stacks, which indicates that the more luminous AGN are likely to be post-starburst systems. The bottom left panel shows  $\text{H}\delta_A$  as a function of  $D_n(4000)$ , where we see that AGN in the

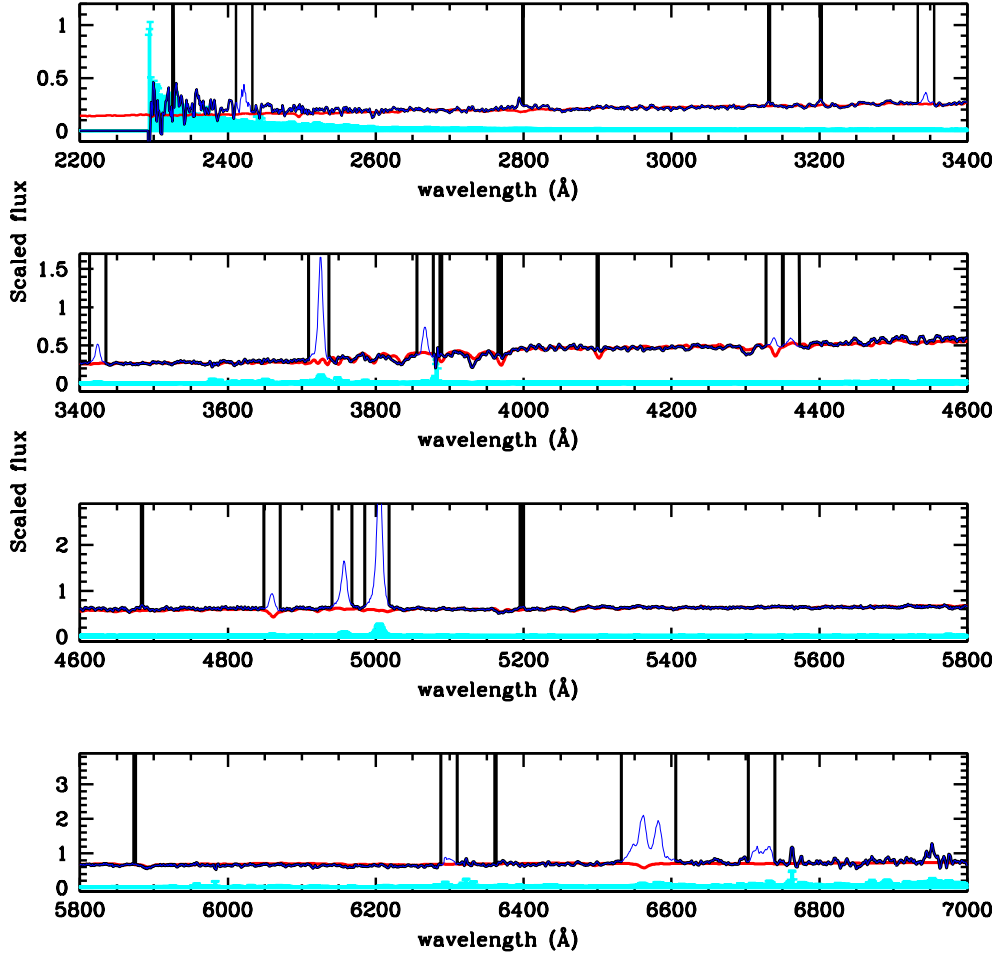


**Figure 2.** An example of a continuum fit is shown in for the stack with  $\log L[\text{OIII}]=8.5$  and mean stellar age between  $6.3 \times 10^8$  and  $1.5 \times 10^9$  Gyr. The stacked spectrum is plotted in black, with vertical black lines delineating masked regions (the actual emission lines in the stacked spectrum are shown in blue). The cyan bands across the bottom of each of the panels indicate the  $\pm 1\sigma$  errors on the mean observed flux. The best fit model spectrum is shown in red. The emission lines that are analyzed in this paper are marked.

two more luminous stacks exhibit the classic signature of enhanced Balmer absorption at fixed 4000 Å break strength (Kauffmann et al 2003a). This finding is consistent with the conclusions presented in Kauffmann (2018) showing that a large fraction of the black hole growth in very luminous AGN takes place in galaxies that have experienced a recent burst of star formation.

The bottom right panel of Figure 3 shows the Balmer decrement ( $H\alpha/H\beta$ ), which is a measure of the dust extinction in the narrow line region, as a function of the 4000 Å break. Note that the dust-free value for case B recombination is 2.86, so there is evidence of dust in these systems. There is, however, very little variation in the measured Balmer decrement with either [OIII] luminosity or with mean stellar age.

In Figure 4, we plot a number of ratios that are sensitive to the ionization state of the gas and the spectral energy distribution of the ionizing radiation field as a function of the mean stellar age of the galaxies in the stack. Once again,

results are shown for 3 different ranges in [OIII] luminosity. The top two panels show the ratios  $[\text{OIII}]\lambda 5007/H\beta$  and  $[\text{OIII}]\lambda 5007/[\text{OII}]\lambda 3727,3729$ . Because the stacks are binned according to [OIII] luminosity, the y-axis separation is to some extent a selection effect. The main conclusion from the upper two panels is that the ionization parameter does not appear to depend on mean stellar age at fixed [OIII] luminosity. When combined with our result that the most luminous AGN tend to have post-starburst stellar populations, we find a clear result that radiation from the black hole rather than from young stars is the dominant source of ionizing photons in these systems. The bottom two panels show the ratios  $[\text{Ne III}]\lambda 3869/[\text{OII}]\lambda 3727,3729$  and  $[\text{Ne V}]\lambda 3345/[\text{Ne III}]\lambda 3869$  as a function of age. Here, the differences between the different [OIII]-luminosity bins are much weaker, and are in the sense of the less luminous AGN having slightly higher ionization or harder-spectrum radiation fields. Once again, there is little or no dependence of these ratios on mean stellar age (the

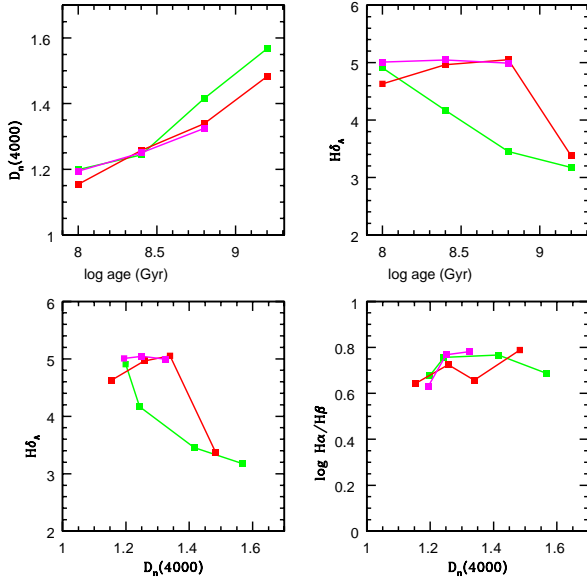


**Figure 3.** *Top:* measured values of  $D_n(4000)$  (left) and  $H\delta_A$  (right) as a function of the logarithm of the mean stellar age. *Bottom left:*  $H\delta_A$  as a function of  $D_n(4000)$ . *Bottom right:* Balmer decrement ( $H\alpha/H\beta$ ) as a function of the 4000 Å break. Each stellar age bin is indicated by a filled square. Results are shown in different colours for the 3 different bins in  $\log L[\text{OIII}]$ : green ( $\log L[\text{OIII}]=8.5-9$ ); red ( $\log L[\text{OIII}]=9-9.5$ ); magenta ( $\log L[\text{OIII}]=9.5-10$ ).

$[\text{NeV}/[\text{NeIII}]$  ratio shows a slight drop for stellar ages greater than  $10^9 M_\odot$ .

We now compare our derived emission line ratios to grids of photo-ionization models provided by Groves, Dopita & Sutherland (2004, hereafter GDS). This comparison is intended to act as a check on our line measurements rather serving as a stringent test of any physical model. As discussed in GDS, the very simplest models assume a constant density of gas and allow for variations in ionization parameter, metallicity and spectral shape of the ionizing radiation field. Constant density models are doubtless oversimplified and take no account for the gas-dynamics of the photo-ionized region. The next level of complexity is to construct simple models with more realistic physics, but that necessarily contain more assumptions. Dopita et al (2002) developed a model for the NLR as a dusty, radiation pressure dominated region surrounding a photo-evaporating molecular cloud, which in turn is surrounded by a coronal halo of gas within which the dust has been largely destroyed. They further assumed that the emission spectrum is generated by the dusty dense inner region near the stagnation point in the flow around the cloud. They argued that this would be the highest emissivity region in the flow, and it would also be the region in which the radiation pressure gradient is matched by the gas pressure gradient, thus allowing for static rather than dynamic photoionization models.

Figure 5 compares derived emission line ratios from our stacked spectra with constant density models. Once again, green, red and magenta squares correspond to measurements from our 3 bins in  $[\text{OIII}]$  line luminosity. There is very little dependence in observed line ratios with stellar age, except

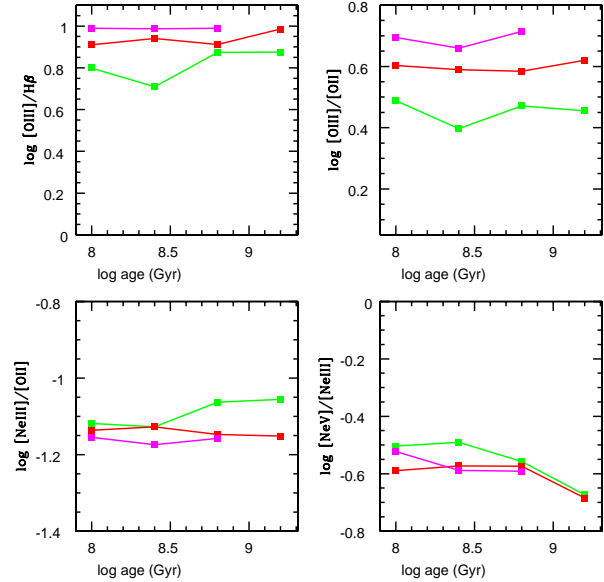


**Figure 4.** A variety of line ratios sensitive to the ionization state of the gas and the spectrum of the ionizing radiation are plotted as a function of the mean age of the stellar population in the host galaxy.

for the case of  $[\text{HeII}]/H\beta$ , which we will discuss in more detail later. Cyan, blue and dark gold open circles correspond to models with metallicities half solar, solar and twice solar, with ionization parameters ranging from  $U=0$  to  $U=-3$ . We adopt a spectral slope  $\alpha = -1.4$ . The models of GDS span a range in spectral slope between  $-1.2$  and  $-2$ , and  $\alpha = -1.4$  is their adopted fiducial value. The measured points lie fairly consistently in the region of model space between the solar and twice solar models with ionization parameter  $U=-2$  (the twice solar model with  $U=-2$  is marked as a blue asterisk in each panel). The only exception are line ratios involving  $[\text{HeII}]\lambda 4386$ . Figure 6 is the corresponding figure for the dusty model. In this case, we see that there is no model that is able to fit the majority of the line ratios consistently. Constraints from the  $[\text{OIII}]\lambda 5007/H\beta$  versus  $[\text{NII}]\lambda 6583/H\alpha$  diagram and the  $[\text{OIII}]\lambda 4363/[\text{OIII}]\lambda 5007$  versus  $[\text{NeV}]\lambda 3426/[\text{NeIII}]\lambda 3866$  diagram would appear to favour models with metallicities between solar and twice solar. In contrast, the  $[\text{OIII}]\lambda 5007/H\beta$  versus  $[\text{OI}]\lambda 6300/H\alpha$  diagram clearly favours models with metallicities near half solar. The fact that we can find a single metallicity that fits most line ratios for the dust-free models and we cannot do the same for the radiation-pressure dominated models may, at first glance, lead us to favour the dust-free models for these very luminous systems. We note, however, that the Balmer decrement values shown in the lower right panel of Figure 3 clearly indicate the presence of dust, so the disagreement may just reflect short-comings in the Dopita et al model for the dynamics of the gas in the narrow-line regions.

Note, however, that both models fail to fit the range in  $[\text{HeII}]\lambda 4386/H\beta$  seen in the stacked spectra. We examine this in more detail in Figure 7, where we plot  $[\text{HeII}]\lambda 4386/H\beta$  as a function of stellar age. Here we see that the

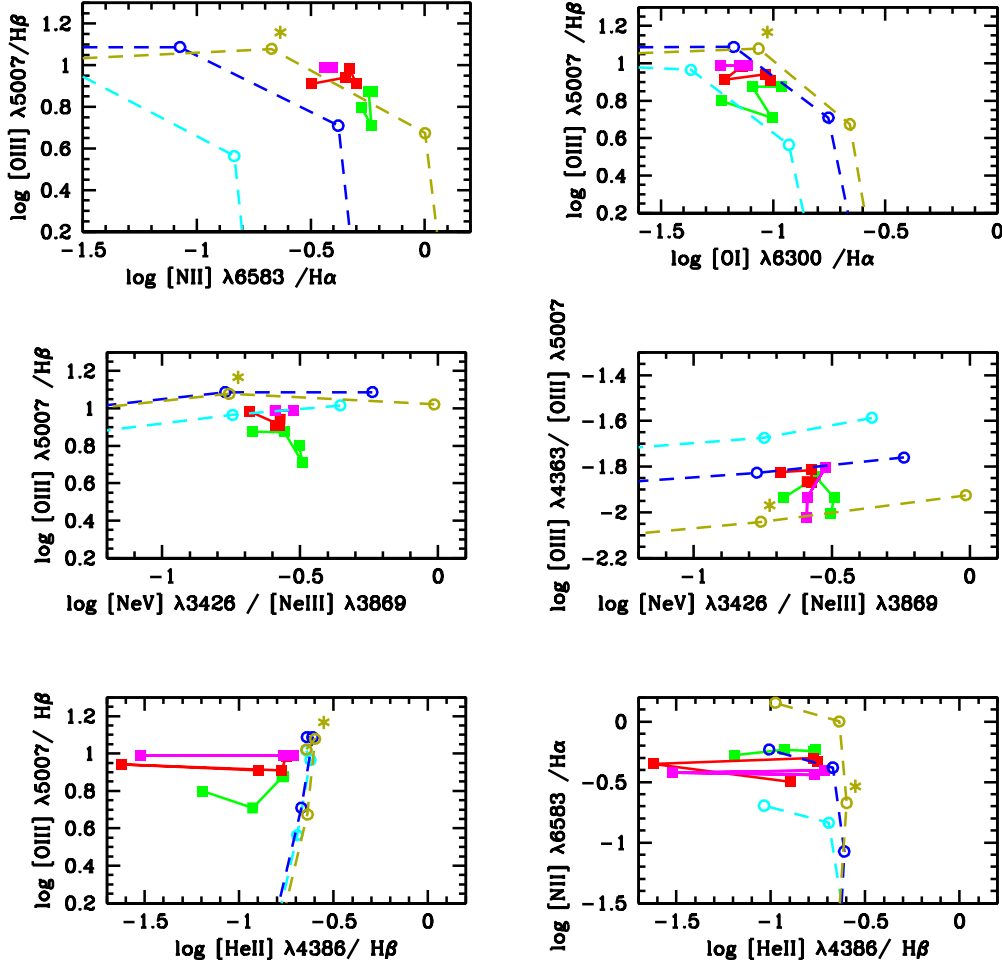


**Figure 5.** Emission line ratios from our stacked spectra are compared with dust-free uniform density photo-ionization models from Groves et al (2014). Green, red and magenta squares correspond to measurements from our 3 bins in [OIII] line luminosity. Cyan, blue and dark gold open circles correspond to models with metallicities half solar, solar and twice solar, with ionization parameters ranging from  $U=0$  to  $U=-3$ . We adopt a spectral slope  $\alpha = -1.4$ . The twice solar model with  $U=-2$  is marked as a dark gold asterisk in each panel.

pronounced “dip” in  $[\text{HeII}]\lambda 4386/\text{H}\beta$  at a stellar age of  $2-5 \times 10^8$  yr in the two high luminosity bins is responsible for the offset from the predictions of the two photo-ionization models. This is the age corresponding to a predominantly post-starburst stellar population in the host galaxies of these AGN. In recent work attempting to reconcile the stellar and nebular spectra of high-redshift galaxies, Steidel et al (2016) examine HeII emission by means of the  $[\text{HeII}]\lambda 1640/\text{H}\beta$  ratio, pointing out that massive star binaries produce a harder ionizing UV spectrum with a different duty cycle than single-star models. We leave further examination of the observed  $[\text{HeII}]$  anomaly in our AGN spectra for future work.

#### 4 EXAMINATION OF EMISSION LINE SHAPES IN NEARBY LUMINOUS AGN

Before proceeding to the results for the stacked spectra, it is instructive to examine high signal-to-noise individual spectra of nearby objects with similar intrinsic luminosities. Stacking will always smooth out features: apparent Gaussian components are likely only Gaussian in shape because we have combined spectra from many galaxies. In this section, we examine some of the strongest emission lines in 8 galaxies with [OIII] luminosities greater than  $10^9 L_{\odot}$  drawn from the sample presented in Kauffmann (2018).

We find that the sources can be split into two main categories. The first category is comprised of sources with clear outflow signatures. There are four such sources and they are shown in Figure 8. The central narrow line component of the [OII] and [OIII] lines are generally blue-shifted with

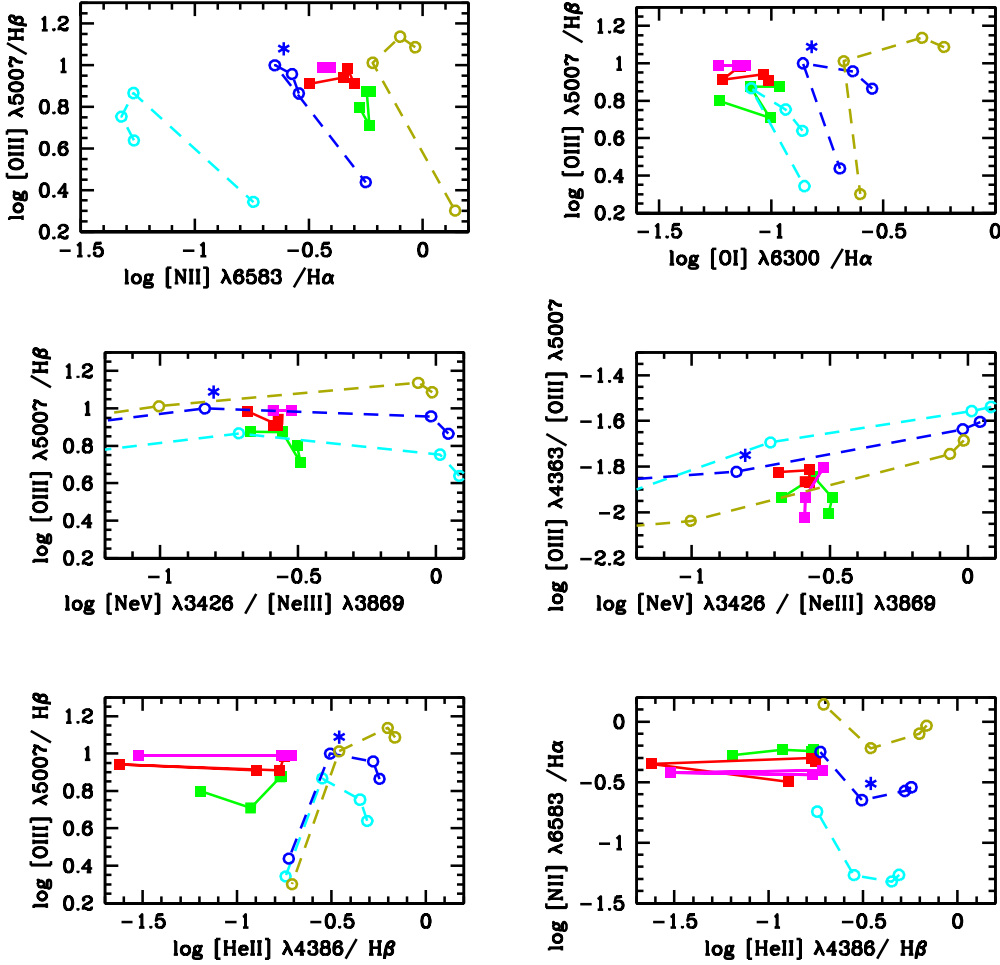


**Figure 6.** As in Figure 5, except for the dusty, radiation pressure dominated photoionization models. Here, the solar model with  $U=-2$  is marked as a blue asterisk.

respect to the systemic velocity (indicated as the dotted vertical line in each panel), and the line shapes are asymmetric with clear blue and/or red-wing excesses seen at the base of the narrow-line component. A blue-side excess is usually also seen in the  $H\alpha$  line. The other four sources in our sample of 8 have double-peaked narrow emission line profiles, but no clear outflow signatures (Figure 9). We note that all of the sources in the sample studied by Kauffmann (2018) are detected in the FIRST VLA radio catalogue and have radio luminosities greater than  $10^{23.5}$  Watts  $\text{Hz}^{-1}$ . It is well-known that radio-loud AGN often exhibit double-peaked narrow emission lines (e.g. Eracleous & Halpern 2003). A variety of scenarios have been proposed to explain these features, including supermassive binary black holes, emission from a bipolar outflow, anisotropically illuminated broad line regions, and illumination of the outer accretion disk by the inner accretion disk.

Interestingly, in our 4 double-peaked sources, the right peak is always centered on the systemic velocity in the case of the [OII] line. For the [OIII] line, the minimum between

the two peaks is centered on the systemic velocity. Double peaks are not seen in the  $H\alpha$  line, except for one case. These systematic differences between different emission line tracers would appear to disfavour the binary black hole hypothesis and favour a scenario where complex radiative transfer effects within a single structure give rise to double peaked line morphologies. For the stacking analysis presented in the next section, our results for individual systems indicate that broad components at the *base* of a central, more narrow emission line, are likely to be indicative of outflows of ionized gas.

## 5 LINE COMPONENT-FITTING RESULTS FOR HIGHER REDSHIFT STACKED SPECTRA

A secondary broad component is detected in all the stacks for the [OIII] $\lambda 4959$ , [OIII] $\lambda 5007$  and  $H\alpha$  lines, and in some stacks for the [OII] $\lambda 3727, 3729$  doublet. A summary of the



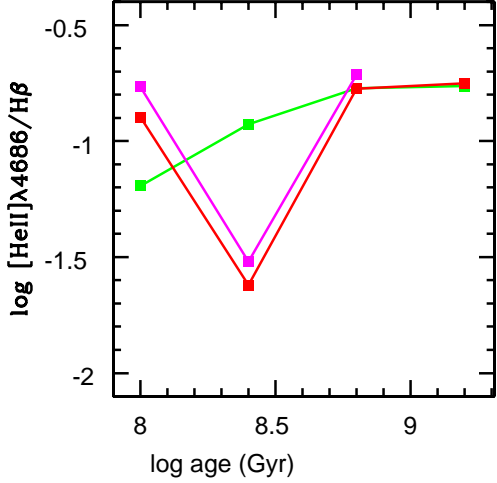


**Figure 7.** Measured values of  $[\text{HeII}]\lambda 4686/\text{H}\beta$  as a function of the logarithm of the mean stellar age. Results are shown in different colours for the 3 different bins in  $\log L[\text{OIII}]$ : green ( $\log L[\text{OIII}]=8.5-9$ ); red ( $\log L[\text{OIII}]=9-9.5$ ); magenta ( $\log L[\text{OIII}]=9.5-10$ ).

properties of the broad components is presented in Table 1. We list the fraction of the total flux contained in the broad component and the velocity widths of the narrow and broad components for each stack. The broad components of the  $[\text{OII}]$  and  $[\text{OIII}]\lambda 5007$  lines have velocity widths of around 500 km/s and contain about a third of the total line flux. We have not yet implemented a formal computation of the errors in these measurements, but examination of the variation between different stacks indicate that the uncertainties are around 50 km/s for the velocity width and 0.05 for the fraction of the flux in the broad component. There is no clear trend in either the velocity width or the broad component fraction with stellar age or with  $[\text{OIII}]\lambda 5007$  line luminosity of the galaxies in the stack. We attribute the fact that the broad  $[\text{OII}]\lambda 3727$  component is not always clearly detected to the fact that the line is a doublet. Also, as shown in the previous section, some sources will be double-peaked, leading to a narrow component in the stack with larger line width. In Table 1, we see that the line width of the narrow component of  $[\text{OII}]\lambda 3727$  is 230-260 km/s compared to 190-210 km/s for the  $[\text{OIII}]\lambda 5007$  line. This means that the contribution from outflowing gas is harder to detect after stacking. The broad components of the  $\text{H}\alpha$  lines in the stacks also contain a third of the total line flux, but are considerably more extended than those of  $[\text{OII}]\lambda 3727$  or  $[\text{OIII}]\lambda 5007$ , with velocity widths of 750-950 km/s. Once again, there is no clear trend in the widths of these broad components with stellar age or  $[\text{OIII}]\lambda 5007$  line luminosity.

In Figures 10, 11 and 12 we illustrate our fits to the lines in the stacked spectra for three different cases: a) the  $[\text{NeIII}]\lambda 3869$  line, for which only one component is detected in all cases (Figure 10), b) the  $[\text{OIII}]\lambda 5007$  line, for which a broad component is always detected (Figure 11), c) the  $\text{H}\alpha$  and  $[\text{NII}]\lambda 6584$  line complex (Figure 12). We show results for the  $\log L[\text{OIII}]=9.0-9.5$  bin for three different ranges in stellar age. In the top row, we show results for the full stacks,

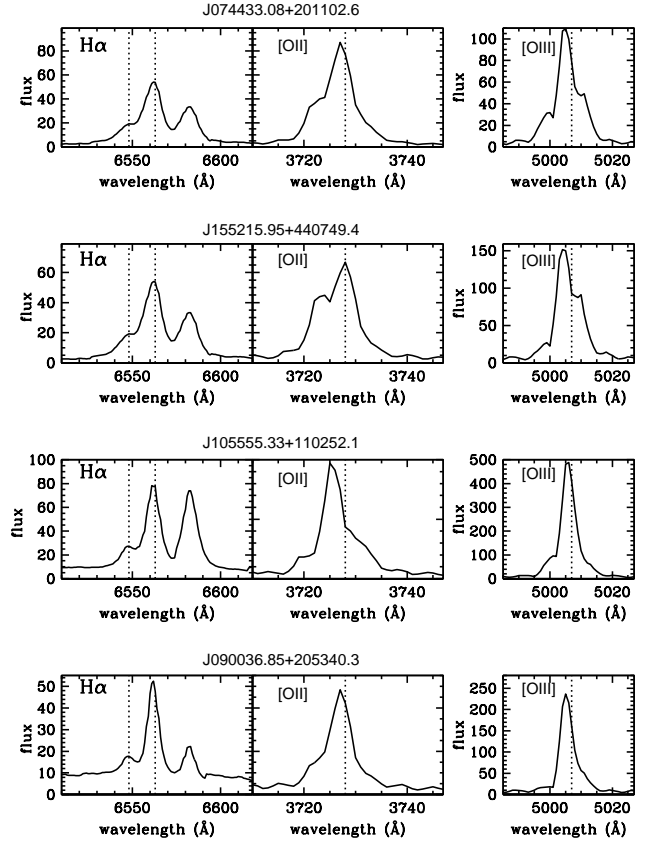


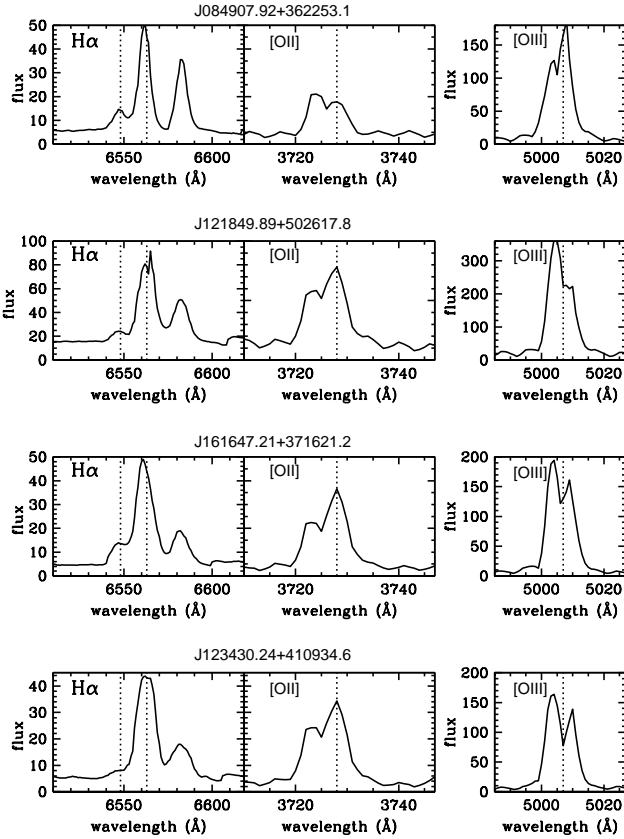
**Figure 8.** Four examples of nearby AGN with  $[\text{OIII}]\lambda 5007$  line luminosities greater than  $10^9 L_{\odot}$  from the sample of Kauffmann (2018) with clear signatures of outflowing gas. We plot the spectra in the vicinity of the  $\text{H}\alpha$ ,  $[\text{OII}]\lambda 3727, 3729$  and  $[\text{OIII}]\lambda 5007$  lines. The vertical dotted lines in the left panels show the expected location of  $\text{H}\alpha$  and  $[\text{NII}]\lambda 6548$  with no systemic shift. In the middle and right panels, we mark  $\lambda = 3728\text{\AA}$  and  $\lambda = 5007\text{\AA}$ .

in the middle row for stacks of radio-detected sources with the same  $[\text{OIII}]\lambda 5007$  luminosity and age, and in the bottom row for stacks of WISE-detected sources. In Figure 10 and 11, the solid black curves show the emission lines in the stacked spectra and the solid red curves the final fit. In the case of a two component fit, the broad component is shown as a dashed magenta curve, while the narrow component is shown as a dashed red curve. The cyan shaded region indicates the errors on the flux in the stacked spectrum, estimated through a bootstrap resampling technique.

Examining Figures 10 and 11, we see that the  $[\text{NeIII}]\lambda 3869$  and  $[\text{OIII}]\lambda 5007$  profiles for the radio and WISE-detected subsamples are very similar to those of the full sample at fixed luminosity and stellar age. The radio-detected subsample shows evidence for complex structure in the narrow component, particularly at young stellar ages. We do not find any systematic quantitative differences between the broad components of the radio-loud and WISE-detected subsamples, showing that the large-scale ionized gas outflows in these systems are identical to those in the luminous AGN population as a whole. This result does not support claims that

**Table 1.** Table of line component quantities. The three quantities listed in each column are, 1) fraction of flux in broad component, 2)  $\sigma$  of narrow component (km/s), 3)  $\sigma$  of broad component (km/s). ND means non-detection of the broad component.

log L[OIII]	log age(Gyr)	OIII $\lambda$ 3727	OIII $\lambda$ 4959	OIII $\lambda$ 5007	H $\alpha$ $\lambda$ 6563
8.5	8.0	ND	0.33007; 199.88; 502.86	0.34719; 209.79; 557.97	0.34075; 241.33; 866.82
8.5	8.4	0.17494; 224.91; 633.39	0.32681; 186.00; 467.96	0.34723; 197.94; 526.53	0.41579; 182.60; 948.53
8.5	8.8	ND	0.32078; 190.97; 457.97	0.34723; 197.94; 526.53	0.31070; 301.12; 920.78
8.5	9.2	ND	0.32019; 196.80; 471.88	0.31954; 202.52; 475.54	0.34829; 245.36; 925.00
9.0	8.0	0.28912; 235.64; 479.79	0.33986; 188.18; 495.71	0.34053; 197.95; 511.12	0.32350; 180.60; 804.34
9.0	8.4	0.29682; 233.81; 494.28	0.32910; 204.49; 514.51	0.34052; 202.52; 522.96	0.30507; 263.61; 759.21
9.0	8.8	0.28125; 232.45; 455.11	0.32971; 197.91; 497.96	0.43324; 207.10; 502.47	0.29143; 302.80; 818.22
9.0	9.2	ND	0.29593; 193.73; 418.78	0.26940; 202.88; 492.20	0.33236; 252.34; 861.52
9.5	8.0	0.27305; 257.81; 484.61	0.30817; 221.44; 504.90	0.31222; 230.02; 522.14	0.33023; 270.15; 922.21
9.5	8.4	0.26478; 250.48; 451.39	0.30803; 224.52; 511.94	0.29461; 220.66; 500.89	0.30071; 319.04; 918.85
9.5	8.8	ND	0.33058; 192.15; 483.51	0.32668; 201.02; 487.62	0.34838; 256.52; 967.16

**Figure 9.** Four examples of nearby AGN with [OIII] line luminosities greater than  $10^9 L_{\odot}$  from the sample of Kauffmann (2018) with double-peaked narrow line profiles. We plot the spectra in the vicinity of the H $\alpha$ , [OIII] $\lambda$ 3727,3729 and [OIII] $\lambda$ 5007 lines. The vertical dotted lines are the same as in Figure 8.

that radio jets are critical feedback mechanisms acting on the ionized gas in massive galaxies (Jarvis et al 2019).

It is also worth noting that the non-detection of a broad component of the [NeIII] $\lambda$ 3869 line is not likely to be a consequence of the fact that this line is weaker in flux than

[OIII] $\lambda$ 5007. A broad component of the [NeIII] line of one third of the total flux would be of the same magnitude as other well-detected lines in the stacks. The more likely explanation is that the outflowing gas traced by [NeIII], which has higher ionization potential than [OIII], is confined closer to the nucleus of the galaxy and cannot be distinguished from the narrow-line region gas. As we will now show, H $\alpha$ , which traces the coolest and densest gas, exhibits the most extended broad component.

Our fits to the H $\alpha$ /[NII] complex are carried out in a series of steps. In Figure 12, the truncation in the H $\alpha$  line redwards of the peak delineates the wavelength region over which the fit is performed. Once again, the solid red curve shows the full fit, while the dashed red and magenta curves show contributions from the narrow and broad components, respectively. The solid magenta curve shows the best single Gaussian fit to the [NII] $\lambda$ 6584 line after the broad component of the H $\alpha$  line is subtracted. As can be seen, two Gaussians for H $\alpha$  plus a single Gaussian for [NII] provide a good fit to the line complex as a whole. A net blue side excess is visible in most of the stacks. The fact that a net blue side excess is seen only for H $\alpha$  stack and not for the [OIII] stack is likely explained by the fact that H $\alpha$  traces cooler, denser gas whose emission is more affected by dust obscuration.

A number of quantitative measures of the H $\alpha$  blue wing excess are provided in Table 2 for each stacked spectrum. We define the blue excess region as the contiguous wavelength region over which the measured line flux remains  $1\sigma$  above the flux given by the best-fit, two-component Gaussian model. We tabulate the minimum wavelength of this region, the corresponding velocity separation of the minimum with respect to the systemic velocity, and the fraction of the broad line component flux that is in the blue excess. The latter is obtained by subtracting the best-fit model flux from the measured flux, summed over the wavelength region that spans the blue excess. The typical velocity separations are around  $\sim 1000$  km/s, with a scatter of  $\sim 200$  km/s between different stacks in a given luminosity bin. The scatter between the measurements of the blue excess fraction between different stacks in the same luminosity bin is  $\sim 0.02$ . There are indications that lower luminosity AGN have larger H $\alpha$  blue excess fractions, even though the maximum blue shift of this component is not larger than for the higher luminosity

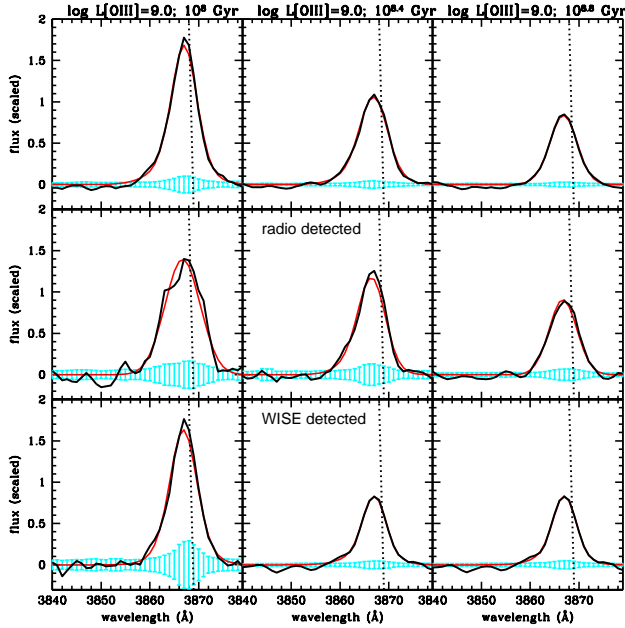


**Figure 10.** Illustration of fits to the  $[\text{NeIII}]\lambda 3869$  line for stacked spectra from our high redshift sample in the  $L[\text{OIII}]=10^9 L_{\odot}$  line luminosity bin at three different stellar ages. The solid back curve shows the stacked spectra and the red curve is the single Gaussian fit. The middle and lower panels compare results for stacked spectra of radio and WISE detected galaxies with the same  $[\text{OIII}]$  luminosities and stellar ages as those in the full sample. The cyan shaded region indicates the errors on the flux in the stacked spectrum, estimated through a bootstrap technique. The vertical dotted line shows  $\lambda = 3869\text{\AA}$

AGN. We note that we have not attempted to subtract the contribution from  $[\text{NII}]\lambda 6548$ . This line is so heavily blended with the  $\text{H}\alpha$  line that any attempt to do so would need to assume that there is a fixed relation with the  $[\text{NII}]\lambda 6583$  line. The blue excess fractions should thus be taken as upper limits and attention given to relative trends rather than absolute values for this quantity.

So far, we successfully identified broad components in stacked spectra, but we have not found significant variation in the properties of this component with AGN luminosity, stellar age, radio or dust emission properties. Although the galaxies in our sample span a rather restricted range in stellar mass, it is still possible to split the sample into two well-separated stellar mass ranges for the most populated bins. We note that  $[\text{OIII}]$  is the highest S/N line in all the stacks. In Figure 13, we show results for AGN with  $\log L[\text{OIII}]=9.0-9.5$  and stellar ages  $\log \text{age} = 8.4-8.8$ . Results for stellar masses in the range  $3 \times 10^{10} - 10^{11} M_{\odot}$  are shown in the left panel and for masses greater than  $3 \times 10^{11} M_{\odot}$  in the right panel. As can be seen from Figure 1, these mass ranges lie on the tails of our stellar mass distribution and we are thus only able to show results for our most populated  $[\text{OIII}]$  luminosity and stellar age bin. We find a 40% difference in the width of the broad component for the two subsamples. The fact that the width of the broad component is more dependent on the potential well depth of the host galaxy than it is on stellar age,  $[\text{OIII}]$ , radio or mid-IR luminosity,

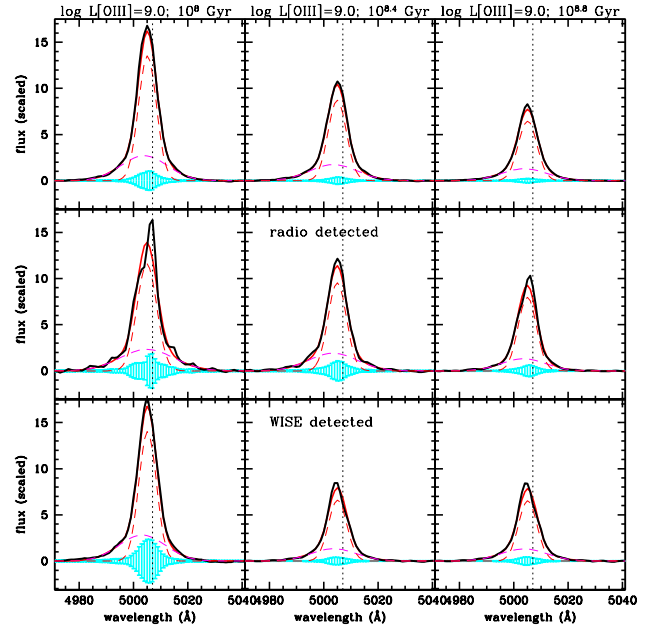


**Figure 11.** Illustration of fits to the  $[\text{OIII}]\lambda 5007$  line for stacked spectra in the  $\log L[\text{OIII}]=9$  line luminosity bin at three different stellar ages. The solid back curve shows the stacked spectra and the solid red curve is the double Gaussian fit. The broad component is shown as a dashed magenta curve, while the narrow component is shown as a dashed red curve. The middle and lower panels compare results for stacked spectra of radio and WISE detected galaxies with the same  $[\text{OIII}]$  luminosities and stellar ages as those in the full sample. The cyan shaded region indicates the errors on the flux in the stacked spectrum, estimated through a bootstrap technique. The vertical dotted line shows  $\lambda = 5007\text{\AA}$

suggests that the galaxy halo plays a crucial role in regulating the kinematics of the outflowing ionized gas, most likely via gravitational confinement and processes such as shock-heating and virialization. Alternatively, it could also mean that the mass of the black hole, which is well-correlated with the stellar mass of the galaxy, is the determining factor. We will come back to these issues in the next section.

## 6 SUMMARY AND CONCLUSIONS

We have carried out a systematic analysis of the emission line properties of Type II AGN at redshifts between 0.4-0.8 with  $[\text{OIII}]$  luminosities greater than  $3 \times 10^8 L_{\odot}$ , i.e systems with luminosities characteristic of the Type II quasars first identified in population studies by Zakamska et al. (2003). These luminous AGN are drawn from the CMASS sample of galaxies that were studied as part of the Baryon Oscillation Spectroscopic Survey (BOSS) survey of galaxies with stellar masses greater than  $10^{11} M_{\odot}$ , and comprise 0.5% of the total population of galaxies at these redshifts. Individual spectra have low S/N, so our analysis is carried out on stacked spectra in bins of  $[\text{OIII}]$  luminosity and stellar age.

Our main findings are the following:

- The emission line ratios of the stacks are remarkably well-fit with simple uniform-density photo-ionization models

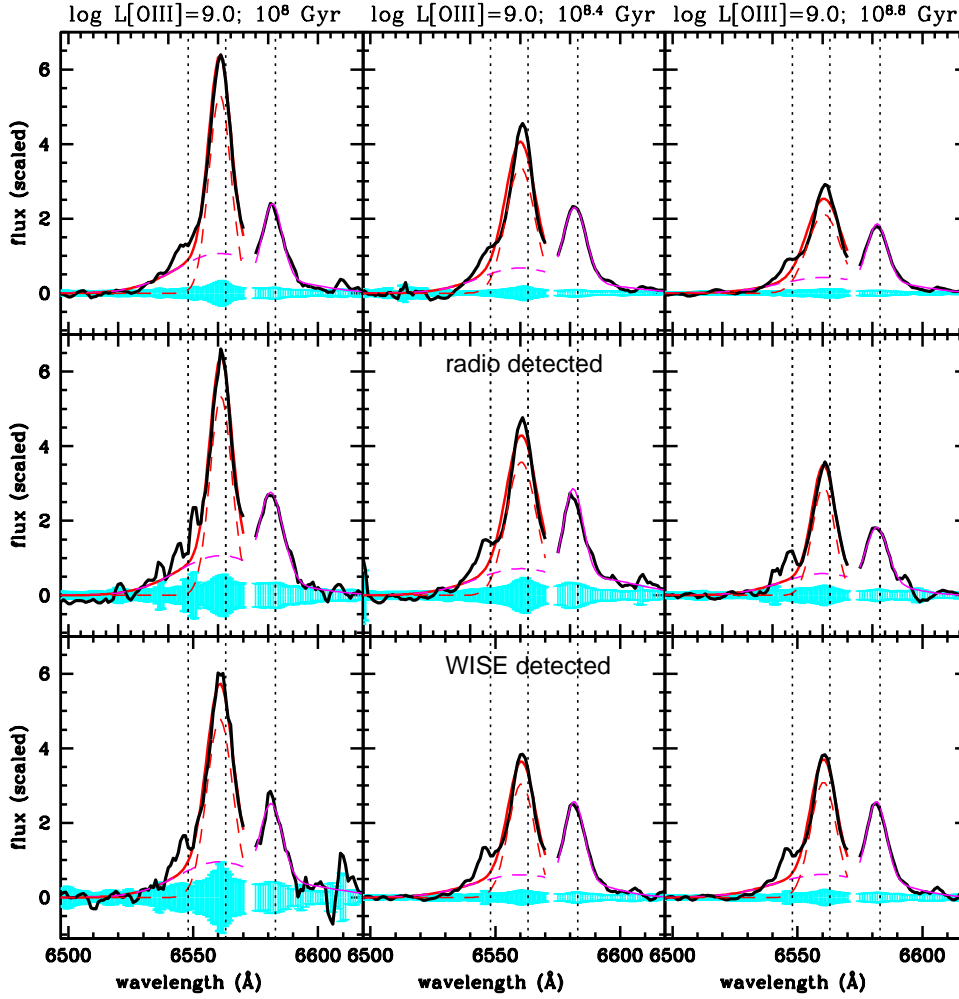


**Figure 12.** Illustration of fits to the H $\alpha$  line for stacked spectra in the  $\log L[\text{OIII}]=9$  line luminosity bin at three different stellar ages. The solid black curve shows the stacked spectra. The solid red curve is the double Gaussian fit, with the broad component shown as a dashed magenta curve and the narrow component as a dashed red curve. The solid magenta curve shows the single Gaussian fit to  $[\text{NII}]\lambda 6583$ . The middle and lower panels compare results for stacked spectra of radio and WISE detected galaxies with the same  $[\text{OIII}]$  luminosities and stellar ages as those in the full sample. The cyan shaded region indicates the errors on the flux in the stacked spectrum, estimated through a bootstrap technique. The three vertical dotted lines mark the  $\lambda = 6548\text{\AA}$   $[\text{NII}]$  line and the rest-frame wavelengths of H $\alpha$  and  $[\text{NII}]\lambda 6583$ .

**Table 2.** Table of quantities pertaining to the blue excess seen in the H $\alpha$  line.

$\log L[\text{OIII}]$	$\log \text{age}(\text{Gyr})$	$\lambda(\text{blue}) \text{\AA}$	$V(\text{blueshift}) \text{ km/s}$	$F(\text{blue})/F(\text{H}\alpha)$
8.5	8.0	6544	871	0.077
8.5	8.4	6536	1239	0.081
8.5	8.8	6536	1239	0.118
8.5	9.2	6536	1239	0.071
9.0	8.0	6540	1055	0.0520
9.0	8.4	6530	1516	0.0465
9.0	8.8	6537	1193	0.0598
9.0	9.2	6437	1193	0.0973
9.5	8.0	6538	1147	0.0427
9.5	8.4	6531	1469	0.0367
9.5	8.8	6538	1147	0.0583

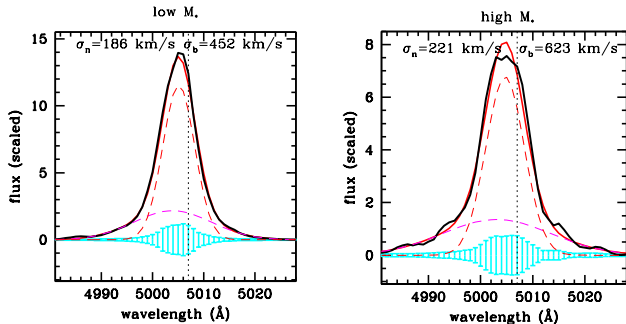


**Figure 13.** Illustration of fits to the [OIII] $\lambda$ 5007 line for stacked spectra in the  $\log L[\text{OIII}]=9$  line luminosity bin and stellar ages  $\log \text{age} = 8.4\text{--}8.8$ . Results for stellar masses in the range  $3 \times 10^{10} - 10^{11} M_{\odot}$  are shown in the left panel and for masses greater than  $3 \times 10^{11} M_{\odot}$  in the right panel. The figure format is the same as in Figure 11.

with power-law ionizing spectra and metallicities between solar and twice solar. The only line ratio that is found to be significantly anomalous is [HeII] $\lambda$ 4686/H $\beta$ , but only in the most luminous AGN at a stellar age of a few times  $10^8$  years. The stellar continuum in these objects shows very prominent post-starburst features.

- In the stacks, a number of emission lines are found to have distinct, well-detected broad components requiring a double Gaussian rather than a single Gaussian fit. These are: [OIII] $\lambda$ 4959, [OIII] $\lambda$ 5007, [OII] $\lambda$ 3727,3729 and H $\alpha$  $\lambda$ 6563. Higher ionization potential lines such as [NeIII] and [NeV] are detected in the stacks, but well-fit by single Gaussians with small net blue-shifts.

- A net blue-side excess after double Gaussian fitting is detected in the H $\alpha$  stack but not in the [OII] or [OIII] stacks.

- In the stacks, the detected broad components always contain a third of the total line flux.

- The width of the broad component is  $\sim 500 - 700$  km/s for the [OII] and [OIII] lines and  $\sim 750 - 950$  km/s for H $\alpha$ .

- The fraction of the flux in the broad component and its width are independent of [OIII] luminosity, stellar age, radio and mid-IR luminosity.

- The only parameter we have identified in this study that appears to influence the width of the broad component is the stellar mass of the galaxy  $M_*$ .

The strongest evidence that the broad components are related to outflowing gas on large scales rather than gas in the accretion disk near the black hole (so called broad-line region (BLR) gas) comes from the fact that the stellar continuum in all the stacks are well fit using linear combinations of simple stellar populations. We performed the experiment of allowing for a featureless power-law component to model a possible contribution from the accretion disk and this did not improve our fits. We also checked for coronal Fe lines and did not find any clear detections. Finally, the lack of a clear broad component in the higher ionization potential [NeIII] and [NeV] lines also disfavours the hypothesis that we are seeing BLR gas in these systems.

Stacking together many different galaxy spectra has the disadvantage of washing out complexity. As we have discussed in Section 1, IFU studies reveal complex, multi-phase

outflows with significant spatial and velocity structure in individual systems. Nevertheless, the hope is that stacking may also yield a number of simple conclusions that provide some degree of physical insight.

One conclusion that has emerged from multi-phase studies of individual systems, such as the study of the molecular and ionized components of the AGN-driven outflow in zC400528, a massive, main sequence galaxy at  $z=2.3$  in the process of quenching (Herrera-Camus et al 2019), is that although the molecular outflow dominates the mass and energy budget, most of the gas does not reach very high velocities. Our study confirms the result shown in Figure 3 of this paper that H $\alpha$  effectively probes gas located in the tails of the velocity distribution ( $\pm 500 - 1000$  km/s), well-separated from the systemic velocity of the galaxy. It is interesting that these high velocity tails are not seen in the higher-ionization lines, suggesting that there may be a “sweet spot” in gas density and temperature for probing such material and that H $\alpha$  may be the most effective tracer.

Another conclusion in need of an explanation is the lack of correlation between the properties of the broad ionized gas component and properties such as AGN luminosity, mean stellar age, and whether or not the galaxy is detected at radio or mid-IR wavelengths. For AGN molecular outflows, Veilleux et al (2013) find that while the outflow velocities show no statistically significant dependence on star formation rate, they are distinctly more blue-shifted among systems with larger AGN luminosity. Perna et al (2017) find a weak correlation between outflow velocity and AGN luminosity for a sample of X-ray selected AGN. We caution that our study is restricted to massive galaxies ( $\log M_* \gtrsim 11$ ), which reside in dark matter halos that are massive enough to contain quasistatic hot gas atmospheres. In such a situation, the AGN-driven wind may be largely confined by the pre-existing gas in the halo and the ionized gas kinematics on large scales may partially reflect virial motions of the halo gas.

Recent work by Nelson et al (2019) on outflows in simulated galaxies has emphasized how the relative simplicity of model inputs (and scalings) at the injection scale produces complex behavior at galactic and halo scales. In their simulations, however, the outflow velocities at injection increase strongly with  $M_*$ , and those measured on galactic scales increase only slightly more weakly, suggesting that some memory of the physical processes at injection should be retained. We caution that in these simulations there is no attempt to link outflow properties with the energetic output from AGN in the form of radiation, so it would be difficult to make robust comparisons with the data. Observationally, separating the physics at the wind injection scale from the physics on halo scales will likely require well-resolved studies of large samples of galaxies spanning a wide range in stellar mass and also multi-phase information about the gas. This is certainly a very significant observational challenge for the future.

### Acknowledgments

We thank Dylan Nelson for useful comments.

### REFERENCES

Alam S., et al., 2015, ApJS, 219, 12

- Antonucci R., 1993, *ARA&A*, 31, 473
- Baldwin J. A., Phillips M. M., Terlevich R., 1981, *PASP*, 93, 5
- Balogh M. L., Morris S. L., Yee H. K. C., Carlberg R. G., Ellingson E., 1999, *ApJ*, 527, 54
- Becker R. H., White R. L., Helfand D. J., 1995, *ApJ*, 450, 559
- Binette L., Wilson A. S., Storch-Bergmann T., 1996, *A&A*, 312, 365
- Bolton A. S., et al., 2012, *AJ*, 144, 144
- Cappellari M., Emsellem E., 2004, *PASP*, 116, 138
- Charlot S., Fall S. M., 2000, *ApJ*, 539, 718
- Chen Y.-M., et al., 2012, *MNRAS*, 421, 314
- Chen C.-T. J., et al., 2017, *ApJ*, 837, 48
- Davies R. L., et al., 2019, *ApJ*, 873, 122
- Dopita M. A., Groves B. A., Sutherland R. S., Binette L., Cecil G., 2002, *ApJ*, 572, 753
- Eracleous M., Halpern J. P., 2003, *ApJ*, 599, 886
- Förster Schreiber N. M., et al., 2019, *ApJ*, 875, 21
- Fluetsch A., et al., 2019, *MNRAS*, 483, 4586
- Genzel R., et al., 2011, *ApJ*, 733, 101
- Groves B. A., Dopita M. A., Sutherland R. S., 2004, *ApJS*, 153, 75
- Groves B. A., Dopita M. A., Sutherland R. S., 2004, *ApJS*, 153, 9 (GDS)
- Harrison C. M., et al., 2017, *MNRAS*, 467, 1965
- Herrera-Camus R., et al., 2019, *ApJ*, 871, 37
- Jarvis M. E., et al., 2019, *MNRAS*, 485, 2710
- Kauffmann G., et al., 2003a, *MNRAS*, 341, 33
- Kauffmann G., et al., 2003b, *MNRAS*, 346, 1055
- Kauffmann G., 2018, *MNRAS*, 480, 3201
- Kroupa P., 2001, *MNRAS*, 322, 231
- Liu G., Zakamska N. L., Greene J. E., Nesvadba N. P. H., Liu X., 2013, *MNRAS*, 436, 2576
- Liu G., Zakamska N. L., Greene J. E., Nesvadba N. P. H., Liu X., 2013, *MNRAS*, 430, 2327
- Maraston C., Nieves Colmenárez L., Bender R., Thomas D., 2009, *A&A*, 493, 425
- Maraston C., Strömbäck G., 2011, *MNRAS*, 418, 2785
- Nelson D., et al., 2019, *arXiv*, arXiv:1902.05554
- Osterbrock D. E., 1989, *agna.book*,
- Padmanabhan N., Xu X., Eisenstein D. J., Scalzo R., Cuesta A. J., Mehta K. T., Kazin E., 2012, *MNRAS*, 427, 2132
- Perna M., Lanzuisi G., Brusa M., Mignoli M., Cresci G., 2017, *A&A*, 603, A99
- Rodríguez-Merino L. H., Chavez M., Bertone E., Buzzoni A., 2005, *ApJ*, 626, 411
- Rose M., Tadhunter C., Ramos Almeida C., Rodríguez Zaurín J., Santoro F., Spence R., 2018, *MNRAS*, 474, 128
- Sánchez-Blázquez P., et al., 2006, *MNRAS*, 371, 703
- Sarzi M., et al., 2006, *MNRAS*, 366, 1151
- Schmidt E. O., Oio G. A., Ferreira D., Vega L., Weidmann W., 2018, *A&A*, 615, A13
- Shakura N. I., Sunyaev R. A., 1973, *A&A*, 24, 337
- Steidel C. C., Strom A. L., Pettini M., Rudie G. C., Reddy N. A., Trainor R. F., 2016, *ApJ*, 826, 159
- Talia M., et al., 2017, *MNRAS*, 471, 4527
- Thomas D., et al., 2013, *MNRAS*, 431, 1383
- Toba Y., Bae H.-J., Nagao T., Woo J.-H., Wang W.-H., Wagner A. Y., Sun A.-L., Chang Y.-Y., 2017, *ApJ*, 850, 140
- Vanden Berk D. E., et al., 2001, *AJ*, 122, 549
- Veilleux S., et al., 2013, *ApJ*, 776, 27
- Wild V., Kauffmann G., Heckman T., Charlot S., Lemson G., Brinchmann J., Reichard T., Pasquali A., 2007, *MNRAS*, 381, 543
- Wild V., Charlot S., Brinchmann J., Heckman T., Vince O., Pacifici C., Chevallard J., 2011, *MNRAS*, 417, 1760
- Wilkinson D. M., Maraston C., Goddard D., Thomas D., Parikh T., 2017, *MNRAS*, 472, 4297
- Worthey G., Ottaviani D. L., 1997, *ApJS*, 111, 377
- Wright E. L., et al., 2010, *AJ*, 140, 1868-1881
- Zakamska N. L., et al., 2003, *AJ*, 126, 2125
- Zakamska N. L., et al., 2016, *MNRAS*, 459, 3144